Geology (2017) 45 (10): 915-918.
DOI: https://doi.org/10.1130/G39113.1
Published: August 08, 2017

Intra-Messinian truncation surface in the Levant basin explained by subaqueous dissolution

Z. Gvirtzman[1,2], V. Manzi[3,4], R. Calvo[1], I. Gavrieli[1], R. Gennari[4,5], S. Lugli[6], M. Reghizzi[3], and M. Roveri[3,4]

[1]Geological Survey of Israel, Jerusalem 95501, Israel
[2]Institute of Earth Sciences, Hebrew University, Jerusalem 9190401, Israel
[3]Department of Chemistry, Life, and Environmental Sustainability, University of Parma, 43124 Parma, Italy
[4]ALP (Alpine Laboratory of Palaeomagnetism), Peveragno I-12016 (CN), Italy
[5]Department of Earth Sciences, University of Turin, 10125 Turin, Italy
[6]Department of Chemical and Geological Sciences, University of Modena and Reggio Emilia, 41125 Modena, Italy

ABSTRACT

The Messinian salinity crisis (MSC) is an extreme event in Earth history during which a salt giant (>1 × 10^6 km^3) accumulated on the Mediterranean seafloor within ~640 k.y. Erosional unconformities extending from the continental margins into the deep basins are key features for reconstructing the MSC; however, the nature of the erosional processes and their subaerial versus subaqueous origin are highly controversial. This study focuses on the top erosion surface (TES) in the deep Levant Basin, which is notably flat, truncating a basinward tilted Messinian evaporitic succession. Based on high resolution seismic surveys and wireline logs, we show that (1) the TES is actually an intra-Messinian truncation surface (IMTS) located ~100 m below the Messinian-Zanclean boundary; (2) the topmost, post-truncation, Messinian unit is very different from the underlying salt deposits and consists mostly of shale, sand, and anhydrite; and (3) the flat IMTS is a dissolution surface related to significant dilution and stratification of the water column during the transition from stage 2 to stage 3. Dissolution occurred upslope where salt rocks at the seabed were exposed to the upper diluted brine, while downslope, submerged in the deeper halite-saturated layer, the salt rocks were preserved. The model, which requires a stratified water column, is inconsistent with a complete desiccation of the eastern Mediterranean Sea.

INTRODUCTION

At ca. 6 Ma, water exchange with the Atlantic reduced and the Mediterranean became a giant saline basin where a 2–3-km-thick evaporite body accumulated (Hsü et al., 1973). This extreme event, known as the Messinian salinity crisis (MSC), lasted ~640 k.y. (Roveri et al., 2014b). Still unanswered fundamental questions are whether or not, when and how low, the Mediterranean sea-level dropped during the MSC. The proposed models range from complete desiccation (Hsü et al., 1973), through ~1500 m sea-level drop (e.g., Ryan, 2009), to a moderate (200–500 m) sea-level fall, which did not prevent a continuous connection with the Atlantic (Roveri et al., 2014a; 2016). Largely accepted is a three-stage evolution of the crisis (CIESM, 2008; Roveri et al., 2014b): in stage 1 (~370 k.y.), gypsum

Geology (2017) 45 (10): 915-918.
DOI: https://doi.org/10.1130/G39113.1
Published: August 08, 2017

accumulated in shallow basins; in stage 2 (~50 k.y.) the salinity peaked and halite and minor gypsum quickly accumulated in the deeper basins; in stage 3 (~220 k.y.) gypsum and/or clastic sediments with distinct brackish fauna were deposited in peculiar schizohaline environments (Lago-Mare, i.e., Sea-Lake; Gignoux, 1936). Orszag-Sperber (2006) proposed that during stage 3 shallow brackish lakes were formed at the bottom of the nearly desiccated basin, as well as around its perched margins. Based on the occurrence of normal marine foraminifera within the Lago-Mare deposits of the North-Betic basins, Braga et al. (2006) suggested that brackish environments may have developed locally, while most of the Mediterranean returned to normal marine conditions, whereas Bassetti et al. (2006) interpreted these findings as due to reworking. The most recent hypothesis suggests that the Mediterranean became a deep-water, low-salinity lake/sea connected to the Atlantic Ocean and the Black Sea with little or no sea-level differences (e.g., Roveri et al., 2014a, 2014b, 2014c; Lugli et al., 2015; Marzocchi et al., 2016; Vasiliev et al., 2017).

Here we focus on the top evaporitic unit of the deep Levant Basin and, particularly, on the top erosion surface (TES). The TES forms a strong seismic reflector (Hsü et al., 1973) commonly related to subaerial erosion induced by desiccation of the basin (e.g., Bertoni and Cartwright, 2007; Lofi et al., 2011), though alternative hypotheses implying subaqueous origin have also been suggested (CIESM, 2008; Roveri et al., 2014c). We show that, the strong TES reflector is associated with an ~100-m-thick uppermost Messinian unit, bounded between the TES and the Messinian-Zanclean boundary; in this work we interpret the lithology of the newly recognized unit and discuss its implications on the MSC.

We integrate high-resolution three-dimensional (3-D) seismic surveys with wells drilled in the deep basin (Aphrodite-2, Myra-1, Sara-1) and on the continental shelf (Gad-1, Nir-1, Nir-2). A key for correlation is the Or-South-1 well, located in the paleo Afiq Canyon (Fig. 1), incised across the continental margin and filled by Messinian evaporites. Due to abrupt landward thinning of the evaporites, this correlation would be impossible elsewhere. Technical details about seismic data, enlarged seismic images, lithological interpretation of well logs, well-seismic calibration, and Sr analyses of cuttings are available in the GSA Data Repository[1].

STRATIGRAPHY

The composite seismic section of Figure 2a shows six evaporitic units that are uplifted and truncated landward, as already shown by previous studies (Netzeband et al., 2006; Bertoni and Cartwright, 2006; Gvirtzman et al., 2013; Gvirtzman et al., 2015; Feng et al., 2016). Our new observations suggest that the strong top reflection consists of at least two pairs of negative and positive peaks, spreading over an ~100 m interval defined here as Unit 7 (Figs. 2c–2f), which is clearly identified basinwide (Figs. DR1–DR4 in the Data Repository). Unfortunately, no cuttings are available for Unit 7 in the deep basin wells, but gamma ray and resistivity logs indicate that it consists of alternating anhydrite, sand, and clay layers (Sara-1, Myra-1; Fig. 3) with some halite and limestone in the deepest portion of the basin (Aphrodite-2). The top and base of Unit 7 are characterized by a downward increase in acoustic impedance and positive reflection peaks (red signals in Figures DR2–DR4 and in Figs. 2c–2f), respectively. Miss-ties between reflection peaks and well logs are around 10 m (see the Data Repository).

Geology (2017) 45 (10): 915-918.
DOI: https://doi.org/10.1130/G39113.1
Published: August 08, 2017

Another key observation is that Unit 7 overlies the surface previously termed TES, which turns out to be an intra-Messinian truncation surface (IMTS) cutting progressively into deeper units landward. In Aphrodite-2 (west), Unit 7 overlies Unit 6; in the area of the Sara-Myra seismic survey it overlies Unit 5 and Unit 4. Farther east the entire evaporite section abruptly thins below seismic resolution (Fig. 2a) and the only area where the thinning pattern can be observed is along the Afiq Canyon (Fig. 2b; Fig. DR4); here Unit 7 approximately maintains its thickness, whereas the underlying section is progressively truncated, as testified by Or-South-1well, where Unit 7 directly overlies Unit 1 (Fig. DR4). Cuttings and logs analyses from Or-South-1 indicate that just like in Sara-1 and Myra-1 Unit 7 consists of interbedded anhydrite-siliciclastic deposits (Fig. 3; Hilton, 2001) floored by an angular unconformity, clearly visible in borehole images (Fig. DR5). $^{87}Sr/^{86}Sr$ analyses on anhydrite chips indicates a stage 3 signature, differing from halite samples taken from units 1–5 of Aphrodite-2 and Myra-1, which yield stage1 and 2 values (Fig. 3c). An evaporite-free unit containing Lago-Mare fauna (Derin, 2000) is present above Unit 7 and below the Messinian-Zanclean boundary, suggesting that Unit 7 represents an early phase of stage 3 before the Lago-Mare phase.

Farther landward (e.g., Gad-1 well; Fig. 3), the MSC succession thins below seismic resolution comprising the anhydrite-siliciclastic Mavqiim Formation overlain by the evaporite-free, Lago-Mare, Afiq Formation (Druckman et al., 1995; Buchbinder et al., 2006). Based on the presence of stage 2 clastic evaporites within the Mavqiim Formation in other nearshore wells (Lugli et al., 2013), we suggest that the condensed Mavqiim Formation represents stage 2 and early stage 3 (Unit 7), whereas the evaporite-free Afiq Formation represents the late stage 3 Lago-Mare phase (Fig. 3).

DISCUSSION

Following these findings, we suggest that the anhydrite-shale alternations (Unit 7) and the overlying evaporite-free Lago-Mare facies (Afiq Formation) belong to stage 3 and that the IMTS records the change from the halite-saturated brines of stage 2 (units 1–6), to the gypsum-saturated brines and/or brackish conditions, of stage 3. Moreover, this transition that occurred when salinity dropped below halite saturation perfectly coincides with the flat truncation of salt units in the abyssal plain, raising the possibility that the truncation was caused by dissolution rather than by erosion.

We suggest that dissolution occurred above the chemocline of a stratified water body with a halite-saturated hypolimnion and under-saturated epilimnion (Fig. 4). When the horizontal chemocline crossed the tilted salt units, the up-tilted part of the basin exposed to the diluted under-saturated upper water layer dissolved away, while the down-tilted part of the basin sunken within the halite-saturated lower brine was preserved. Such a model explains the flat truncation in the abyssal plains, where the seafloor is nearly horizontal and the erosional energy (subaqueous and subaerial) is normally negligible. Moreover, the timing of truncation supports the idea that tilting of the continental margin was a flexural response to quick loading of the salt in the basin (Govers et al., 2008); hence it stopped when massive salt deposition terminated.

The idea of water density stratification, with normal seawater overlain by brackish water, could also explain the peculiar Lago-Mare conditions (Marzocchi et al., 2016), in agreement with recent studies that argue against a full Mediterranean desiccation during

stage 3 on the basis of geochemical and paleontological data (Carnevale et al., 2008; Christeleit et al., 2015; Grunert et al., 2016; Vasiliev et al., 2017, Roveri et al., 2008; 2014a,b,c; 2016; Lugli et al., 2015; Cornée et al., 2016; Stoica et al., 2016). In a wider context, our indication for a subaqueous truncation at the transition between stage 2 and 3 represent an additional contribution to the longstanding controversy about the magnitude of the sea-level drop during the MSC. Though subaqueous truncation still does not reveal the exact water depth, it is clearly inconsistent with desiccation, at least, in the eastern Mediterranean.

CONCLUSIONS

The strong reflector marking the top of the MSC evaporites has been considered by generations of researchers as (1) the top of the Messinian evaporites, (2) the Miocene-Pliocene boundary, and (3) the TES in places such as the Levant basin. Integrating new high-resolution seismic and borehole data (cuttings, logs, Sr isotopes) from the Levant basin, we provide new insights on the nature of this seismic feature. We recognize a previously unidentified clastic-rich anhydrite unit below the Messinian-Pliocene boundary and above the erosional surface. Sr isotope analyses suggest that this unit represents stage 3 of the salinity crisis and that the regional truncation of the tilted section occurred at the transition between stage 2 and 3, which marks a significant change in salinity and a water density stratification of the basin. We suggest that a differential truncation was induced by the dissolution of salt upslope, where the seafloor was above the chemocline, while downslope the salt deposits submerged in halite saturated brines were preserved.

ACKNOWLEDGMENTS

We are grateful to Modiin Energy and Pelagic partnership for their permission to release seismic and well data. Comments by Wout Krijgsman, Joe Cartwright, and a third anonymous reviewer are greatly acknowledged.

REFERENCES CITED

Bassetti, M.A., Miculan, P., and Sierro, F.J., 2006, Evolution of depositional environments after the end of Messinian Salinity Crisis in Nijar basin (SE Betic Cordillera): Sedimentary Geology, v. 188–189, p. 279–295, doi:10.1016/j.sedgeo.2006.03.009.

Braga, J.C., Martín, J.M., Riding, R., Aguirre, J., Sánchez-Almazo, I.M., and Dinarès-Turell, J., 2006, Testing models for the Messinian salinity crisis: The Messinian record in Almería, SE Spain: Sedimentary Geology, v. 188–189, p. 131–154, doi:10.1016/j.sedgeo.2006.03.002.

Bertoni, C., and Cartwright, J.A., 2006, Controls on the basinwide architecture of late Miocene (Messinian) evaporites on the Levant margin (Eastern Mediterranean): Sedimentary Geology, v. 188–189, p. 93–114, doi:10.1016/j.sedgeo.2006.03.019.

Bertoni, C., and Cartwright, J.A., 2007, Major erosion at the end of the Messinian Salinity Crisis: Evidence from the Levant Basin, Eastern Mediterranean: Basin Research, v. 19, p. 1–18, doi:10.1111/j.1365-2117.2006.00309.x.

Buchbinder, B., Siman-Tov, R., Grossowicz, L., Calvo, R., and Almogi-Labin, A., 2006, Stratigraphic and environmental analysis of the Gad-1 borehole, Offshore Israel: Geological Survey of Israel, Confidential Report No. GSI/1/2006, 22 p.

Carnevale, G., Longinelli, A., Caputo, D., Barbieri, M., and Landini, W., 2008, Did the Mediterranean reflooding preceded the Mio-Pliocene boundary?: Paleontological and geochemical evidence from upper Messinian sequences of Tuscany, Italy: Palaeogeography, Palaeoclimatology, Palaeoecology, v. 257, p. 81–105, doi:10.1016/j.palaeo.2007.09.005.

Christeleit, E.C., Brandon, M.T., and Zhuang, G., 2015, Evidence for deep-water deposition of abyssal Mediterranean evaporites during the Messinian salinity crisis: Earth and Planetary Science Letters, v. 427, p. 226–235, doi:10.1016/j.epsl.2015.06.060.

CIESM (The Mediterranean Science Commission), 2008, The Messinian Salinity Crisis from mega-deposits to microbiology—A consensus report, *in* Briand, F., ed., CIESM Workshop Monograph 33: Monaco, The Mediterranean Science Commission, 168 p.

Cornée, J.J., Münch, P., Achalhi, M., Merzeraud, G., Azdimousa, A., Quillévéré, F., Melinte-Dobrinescu, M., Chaix, C., Moussa, A.B., Lofi, J., and Séranne, M., 2016, The Messinian erosional surface and early Pliocene reflooding in the Alboran Sea: New insights from the Boudinar basin, Morocco: Sedimentary Geology, v. 333, p. 115–129, doi:10.1016/j.sedgeo.2015.12.014.

Derin, B., 2000, Stratigraphic and environments of deposition of Or South 1075–2090 m: Report 2/00, Internal Isramco Consultant Report, 10 p.

Druckman, Y., Buchbinder, B., Martinotti, G., Siman Tov, R., and Aharon, P., 1995, The buried Afiq Canyon (eastern Mediterranean. Israel): A case study of a Tertiary submarine canyon exposed in Late Messinian times: Marine Geology, v. 123, p. 167–185, doi:10.1016/0025-3227(94)00127-7.

Feng, Y.E., Yankelzon, A., Steinberg, J., and Reshef, M., 2016, Lithology and characteristics of the Messinian evaporite sequence of the deep Levant Basin, eastern Mediterranean: Marine Geology, v. 376, p. 118–131, doi:10.1016/j.margeo.2016.04.004.

Gignoux, M., 1936, Géologie Stratigraphique, 2nd Edition: Paris, Masson.

Govers, R., Meijer, P., and Krijgsman, W., 2008, Regional isostatic response to Messinian Salinity Crisis events: Tectonophysics, v. 463, p. 109–129, doi:10.1016/j.tecto.2008.09.026.

Grunert, P., Harzhauser, M., Rosenthal, Y., and Carnevale, G., 2016, Estuarine Lago Mare fauna from the Tertiary Piedmont Basin indicates episodic Atlantic/Mediterranean exchange during the final stage of the Mediterranean Salinity Crisis: Palaeogeography, Palaeoclimatology, Palaeoecology, v. 457, p. 70–79, doi:10.1016/j.palaeo.2016.06.005.

Gvirtzman, Z., Reshef, M., Buch-Leviatan, O., and Ben-Avraham, Z., 2013, Intense salt deformation in the Levant Basin in the middle of the Messinian Salinity Crisis: Earth and Planetary Science Letters, v. 379, p. 108–119, doi:10.1016/j.epsl.2013.07.018.

Gvirtzman, Z., Reshef, M., Buch-Leviatan, O., Groves-Gidney, G., Karcz, Z., Makovsky, Y., and Ben-Avraham, Z., 2015, Bathymetry of the Levant basin: Interaction of salt-tectonics and surficial mass movements: Marine Geology, v. 360, p. 25–39, doi:10.1016/j.margeo.2014.12.001.

Hilton, V.C., 2001, BG International offshore Israel, Med Yavne license: Or-1 & Or Shouth-1, Structural and sedimentological interpretation of STAR data, core

sedimentology and petrography of core samples: Baker Atlas GEOScience, Final Report # ZSL-00–075, 32 p.

Hsü, K.J., Ryan, W.B.F., and Cita, M.B., 1973a, Late Miocene desiccation of the Mediterranean: Nature, v. 242, p. 240–244, doi:10.1038/242240a0.

Lofi, J., Sage, F., Déverchère, J., Loncke, L., Maillard, A., Gaullier, V., Thinon, I., Gillet, H., Guennoc, P., and Gorini, C., 2011, Refining our knowledge of the Messinian salinity crisis records in the offshore domain through multi-site seismic analysis: Bulletin de la Société Géologique de France, v. 182, p. 163–180, doi:10.2113/gssgfbull.182.2.163.

Lugli, S., Gennari, R., Gvirtzman, Z., Manzi, V., Roveri, M., and Schreiber, B.C., 2013, Evidence of clastic evaporites in the canyons of the Levant Basin (Israel): Implications for the Messinian Salinity Crisis: Journal of Sedimentary Research, v. 83, p. 942–954, doi:10.2110/jsr.2013.72.

Lugli, S., Manzi, V., Roveri, M., and Schreiber, B.C., 2015, The deep record of the Messinian salinity crisis: Evidence of a non-desiccated Mediterranean Sea: Palaeogeography, Palaeoclimatology, Palaeoecology, v. 297, p. 83–99.

Marzocchi, A., Flecker, R., Van Baak, C.G., Lunt, D.J., and Krijgsman, W., 2016, Mediterranean outflow pump: An alternative mechanism for the Lago-mare and the end of the Messinian Salinity Crisis: Geology, v. 44, p. 523–526, doi:10.1130/G37646.1.

Netzeband, G., Hubscher, C., and Gajewski, D., 2006, The structural evolution of the Messinian evaporites in the Levantine Basin: Marine Geology, v. 230, p. 249–273, doi:10.1016/j.margeo.2006.05.004.

Orszag-Sperber, F., 2006, Changing perspectives in the concept of “Lago-Mare” in Mediterranean Late Miocene evolution: Sedimentary Geology, v. 188, p. 259–277, doi:10.1016/j.sedgeo.2006.03.008.

Roveri, M., Bertini, A., Gennari, R., Gliozzi, E., Grossi, F., Iaccarino, S.M., Lugli, S., Manzi, V., Negri, A., and Taviani, M., 2008, A high-resolution stratigraphic framework for the latest Messinian events in the Mediterranean area: Stratigraphy, v. 5, p. 323–342.

Roveri, M., Manzi, V., Bergamasco, A., Falcieri, F., Gennari, R., and Lugli, S., 2014a, Dense shelf water cascading and Messinian canyons: a new scenario for the Mediterranean salinity crisis: American Journal of Science, v. 314, p. 751–784, doi:10.2475/05.2014.03.

Roveri, M., et al., 2014b, The Messinian Salinity Crisis: Past and future of a great challenge for marine sciences: Marine Geology, v. 352, p. 25–58, doi:10.1016/j.margeo.2014.02.002.

Roveri, M., Lugli, S., Manzi, V., Gennari, R., and Schreiber, B.C., 2014c, High-resolution strontium isotope stratigraphy of the Messinian deep Mediterranean basins: Implications for marginal to central basins correlation: Marine Geology, v. 349, p. 113–125, doi:10.1016/j.margeo.2014.01.002.

Roveri, M., Gennari, R., Lugli, S., Manzi, V., Minelli, N., Reghizzi, M., Riva, A., Rossi, M.E., and Schreiber, B.C., 2016, The Messinian salinity crisis: Open problems and possible implications for Mediterranean petroleum systems: Petroleum Geoscience, v. 22, p. 283–290, doi:10.1144/petgeo2015-089.

Geology (2017) 45 (10): 915-918.
DOI: https://doi.org/10.1130/G39113.1
Published: August 08, 2017

Ryan, W., 2009, Decoding the Mediterranean salinity crisis: Sedimentology, v. 56, p. 95–136, doi:10.1111/j.1365-3091.2008.01031.x.

Stoica, M., Krijgsman, W., Fortuin, A., and Gliozzi, E., 2016, Paratethyan ostracods in the Spanish Lago-Mare: More evidence for interbasinal exchange at high Mediterranean sea level: Palaeogeography, Palaeoclimatology, Palaeoecology, v. 441, p. 854–870, doi:10.1016/j.palaeo.2015.10.034.

Vasiliev, I., Mezger, E.M., Lugli, S., Reichart, G.-J., Manzi, V., and Roveri, M., 2017, How dry was the Mediterranean during the Messinian salinity crisis: Palaeogeography, Palaeoclimatology, Palaeoecology, v. 471, p. 120–133, doi:10.1016/j.palaeo.2017.01.032.

Figure 3. A: Stratigraphic correlation section through Aphrodite-2, Myra-1, Sara-1, Or-South, and Gad-1 well (Levant Basin), flattened according to the Intra-Messinian Truncation Surface (IMTS) at the base of Unit 7 (stage 2–3 transition). Note the different vertical scales below and above the IMTS. Lithology in Aphrodite-2, Myra-1, and Sara-1 is based on GR, RES, and ROP (rate of penetration) logs. Lithology in Or-South and Gad-1 is based on wireline logs confirmed by biostratigraphy and sedimentology analyses (Derin, 2000; Hilton, 2001; Buchbinder et al., 2006). The presence of halite within the lower part of Unit 7 in Aphrodite-2 may represent reworking of halite clasts downslope following the initial stage of dissolution. Red circles indicate position of samples for $^{87}Sr/^{86}Sr$ analyses. b) Structural geometry of the MSC section and the Pliocene-Quaternary (P-Q) overburden between studied wells with no flattening and relative to sea-level. C: Results of $^{87}Sr/^{86}Sr$ analyses. Note the clear distinction between stage 1+2 values found in the halite units and stage 3 values found in unit 7 (details about Sr values typical to the three stages of the MSC are presented by Roveri et al. [2014c]). A few intermediate values found in Unit 7 in Or-South probably represent reworked gypsum derived from stage 1 or stage 2 sulfates. Symbols are larger than error bars (2 standard error; min 6 ppm; max 15 ppm; average 9 ppm; further information is provided in the Data Repository [see footnote 1]).

[1]GSA Data Repository item 2017xxx, xxxxxxxx, is available online at http://www.geosociety.org/datarepository/2017/ or on request from editing@geosociety.org.

Geology (2017) 45 (10): 915-918.
DOI: https://doi.org/10.1130/G39113.1
Published: August 08, 2017

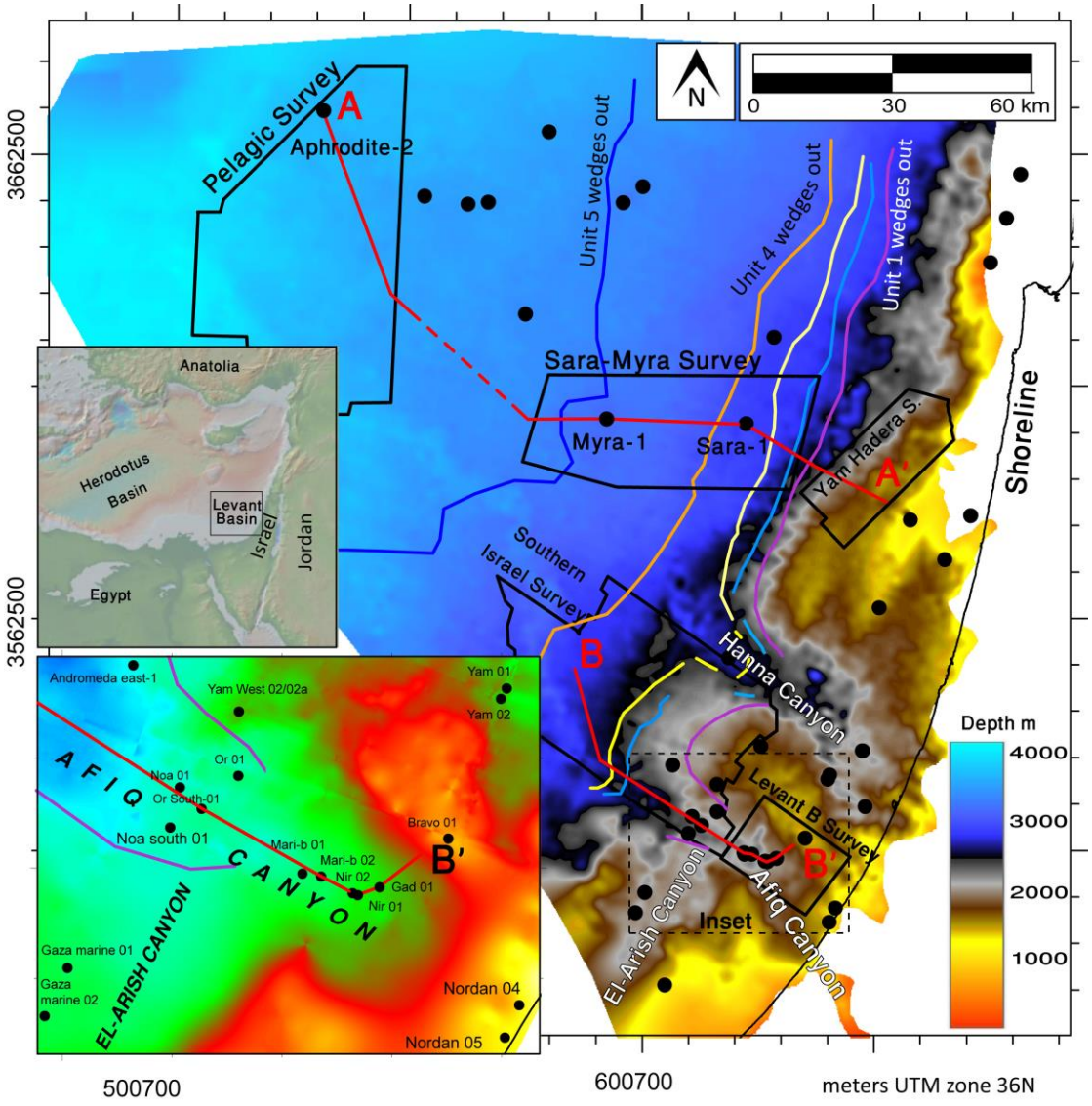

Fig. 1. Location map (Levant Basin). Background is a structural map of the base of the Messinian evaporites. Black dots are wells; black polygons show high resolution seismic surveys. Seismic sections AA' and BB' are shown in Figure 2. Colored lines annotated "Unit 1" to "Unit 5" represent wedge out fronts (thickening westwards). Note that Unit 1 (purple line) penetrates into the Hanna and Afiq canyons. Inset map: Enlargement of the Afiq canyon area with TWT (two way traveltime) map.

Geology (2017) 45 (10): 915-918.
DOI: https://doi.org/10.1130/G39113.1
Published: August 08, 2017

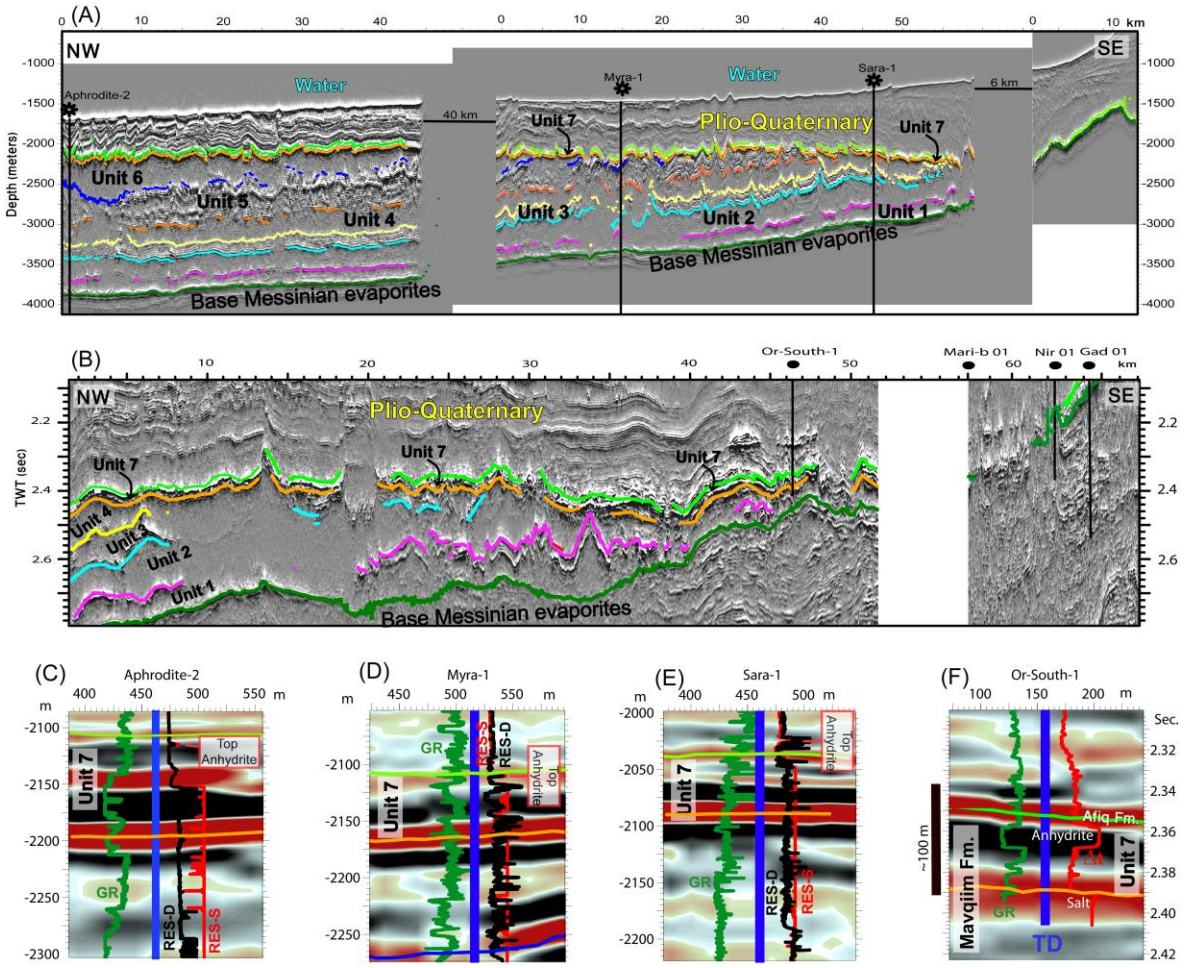

Figure 2. Seismic sections in the Levant Basin. A: Section AA' (location in Fig. 1) from high-resolution pre-stack depth-migrated reflection data showing a basinward-tilted and truncated sequence. The M reflector is composed of two separate lines shown in detail in panels C–F. Subdivision of the Messinian sequence to Units 1–6 follows Gvirtzman et al. (2013). B: Section BB' (location in Fig. 1) composed of high-resolution pre-stack time-migrated reflection data showing gradual thinning of the Messinian sequence through the Afiq Canyon. C–F: Detailed seismic images of Unit 7 with wireline logs from Aphrodite-2, Myra-1, Sara-1, and Or-South, illustrating that the M reflector previously considered as the top evaporitic sequence and Pliocene-Miocene boundary is actually consisting of an ~100-m-thick unit with several distinct layers (see internal stratigraphy in Figure 3). Technical details about tying well logs to seismic reflections, and additional seismic images, are provided in the Data Repository (see footnote 1).

Geology (2017) 45 (10): 915-918.
DOI: https://doi.org/10.1130/G39113.1
Published: August 08, 2017

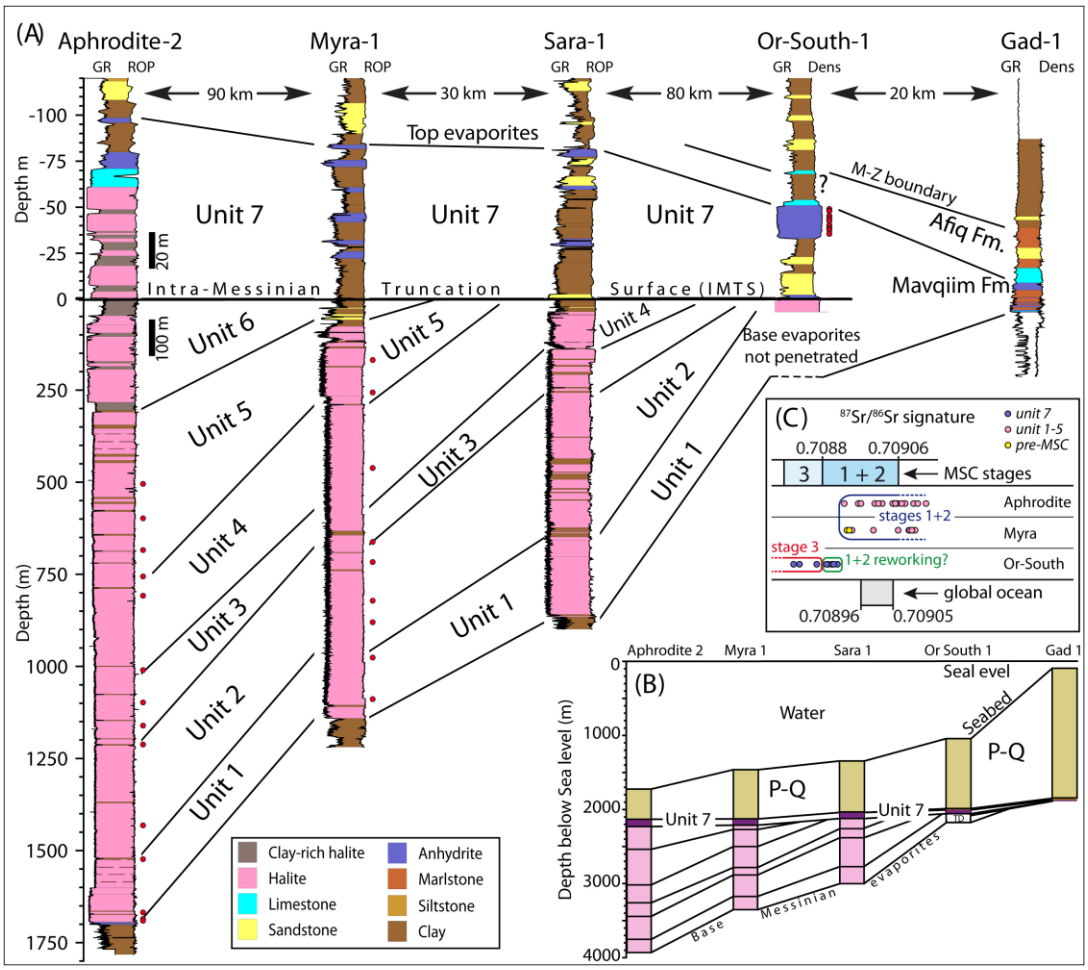

Figure 3. A: Stratigraphic correlation section through Aphrodite-2, Myra-1, Sara-1, Or-South, and Gad-1 well (Levant Basin), flattened according to the Intra-Messinian Truncation Surface (IMTS) at the base of Unit 7 (stage 2–3 transition). Note the different vertical scales below and above the IMTS. Lithology in Aphrodite-2, Myra-1, and Sara-1 is based on GR, RES, and ROP (rate of penetration) logs. Lithology in Or-South and Gad-1 is based on wireline logs confirmed by biostratigraphy and sedimentology analyses (Derin, 2000; Hilton, 2001; Buchbinder et al., 2006). The presence of halite within the lower part of Unit 7 in Aphrodite-2 may represent reworking of halite clasts downslope following the initial stage of dissolution. Red circles indicate position of samples for 87Sr/86Sr analyses. b) Structural geometry of the MSC section and the Pliocene-Quaternary (P-Q) overburden between studied wells with no flattening and relative to sea-level. C: Results of 87Sr/86Sr analyses. Note the clear distinction between stage 1+2 values found in the halite units and stage 3 values found in unit 7 (details about Sr values typical to the three stages of the MSC are presented by Roveri et al. [2014c]). A few intermediate values found in Unit 7 in Or-South probably represent reworked gypsum derived from stage 1 or stage 2 sulfates. Symbols are larger than error bars (2 standard error; min 6 ppm; max 15 ppm; average 9 ppm; further information is provided in the Data Repository [see footnote 1]).

Geology (2017) 45 (10): 915-918.
DOI: https://doi.org/10.1130/G39113.1
Published: August 08, 2017

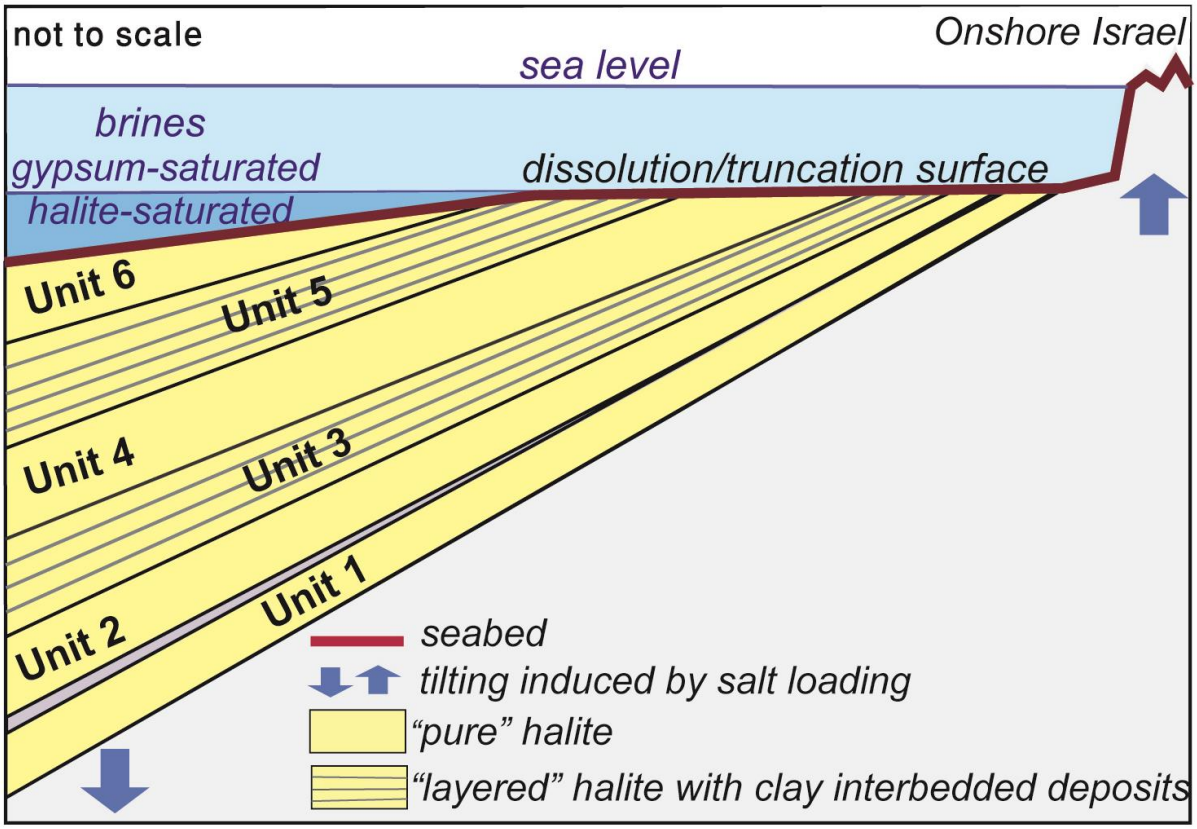

Figure 4. Model for submarine dissolution of a tilted evaporitic sequence above a horizontal chemocline separating a lower halite-saturated hypolimnion from upper under saturated epilimnion.

Supplamentary material for “Intra-Messinian Truncation Surface in the Levant Basin Explained by Suaquaeous Dissolution”

Gvirtzman, Z.[1,2], Manzi, V.[3,4], Calvo, R.[1], Gavrieli, I[1]., Gennari, R[4,5]., Lugli, S[6]., Reghizzi, M.[3], Roveri, M.[3,4]

S1 Log analysis

Due to safety limitations that required riserless drilling until penetrating a few hundred meters within the evaporite section, the topmost part of the section was not sampled in Aprodite-2, Myra-1, and Sara-1. Hence, lithologic interpretation of Unit 7 in these wells is limited to gamma ray (GR) and resistivity (RES) logs acquired while drilling. This interpretation is not as definite as the interpretation of the deeper Messinian units in nearby wells (Feng et al., 2016), which is based on a larger post-drilling log suite (GR, RES, neutron porosity, sonic), but currently this is the only available dataset for the upper part of the evaporitic section in the deep basin.

Our interpretation is based on the following guidelines. Clay units are identified by increased GR, increased penetration rate (soft), and decreased Res with convergence of the “deep” and “shallow” logs (deep and shallow refers to the depth of invasion; convergence indicates impermeable rocks into which drilling fluids cannot invade). Anhydrite is characterized by very low GR and high to very high Res. In halite, GR is very low, Res is very high, and the “deep” Res frequently maxes out forming a “vertical wall” on the edge of the scale (no porosity). Limestone and sandstone have low GR, but usually differ in Res (moderate-low in sandstone and high in limestone) with clear splitting of the “shallow” and “deep” Res logs (permeable). Noteworthy, the interpretation of the Sara-1 and Myra-1 wells according to these guidelines was found consistent with observations from the Or-South-1 well.

S2 Seismic interpretation and tying to well logs

All seismic surveys used in this study were processed in zero phase with SEG normal polarity and, therefore, an increase in acoustic impedance is represented by a positive amplitude peak. Accordingly, the seabed is represented by a positive peak shown by a coherent strong red line at the top of figures DR2a and DR3a and the transition from salt to clays at the base of the evaporites is represented by a negative peak shown by a less coherent, but still quite clear, black signal (marked with a thin green line at the bottom of Figs. DR2a, DR3a). Comparing the measured seabed depth in Aprodite-2, Myra-1, and Sara-1 wells to the depth of the seabed reflection in the pre-stack depth-migrated surveys (Sara-Myra and

Pelagic) shows perfect match with a misstie in order of 1 meter. At the base of the evaporites (reflector N) the mistie is bigger ranging from a few meters in Aprodite-2 to about 40 m in Sara-1 and Myra-1 well sites.

Consistent with these observations, the top of unit 7 (transition from clays to clastic-rich anhydrite rocks) and its base (transition from clastic-rich anhydrites to salt) are both characterized by an increase in acoustic impedance and, therefore, are expected to produce a positive peaks (red). Specific peaking of these two reflectors from the bundle reflections unconformably covering the salt complex is not always simple. Figures DR2-4 show that the two chosen reflectors are quite close (1-10 m) to lithological boundaries shown by well logs, though perfect match is not expected. The base reflector is quite strong and coherent as expected from the top salt boundary, whereas the top reflector is weaker and sometimes vague as expected from thin anhydrite layers interbedded within clays and sands.

#	Survey name	Units	Source	Line Spacing
1	Sara-Myra	Depth m	Modi'in Energy + ILDC	25mX12.5m
2	Yam Hadera	Depth m	Modiin Energy	25mX12.5m
3	Pelagic	Depth m	Pelagic Partnership	25mX25m
4	Isramco Southern Israel	TWT sec	Israel National Archive	12.5mX12.5m
5	Levant B	TWT sec	Israel National Archive	12.5mX12.5m

Table DR1: Technical specifications of 3D seismic surveys. "Sara-Myra", "Yam Hadera", and "Pelagic" are 3D pre-stack depth-migrated (depth scale) surveys. "Southern Israel" and the "Levant B" are 3D time-migrated (two-way-time scale) surveys.

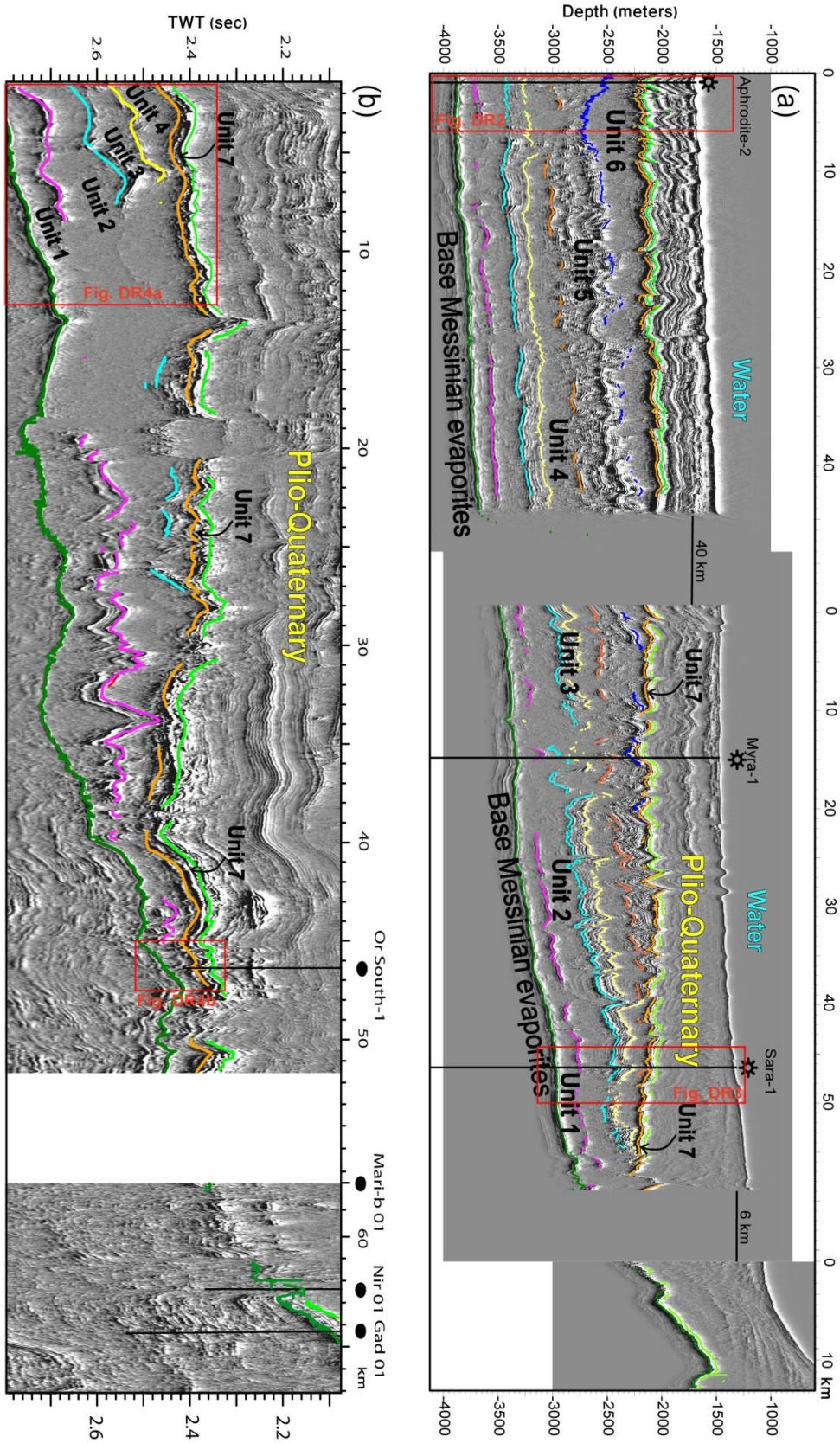

Figure DR1: Enlargement of Figures 2a-b with red frames marking further enlargements shown in Figures DR2-4.

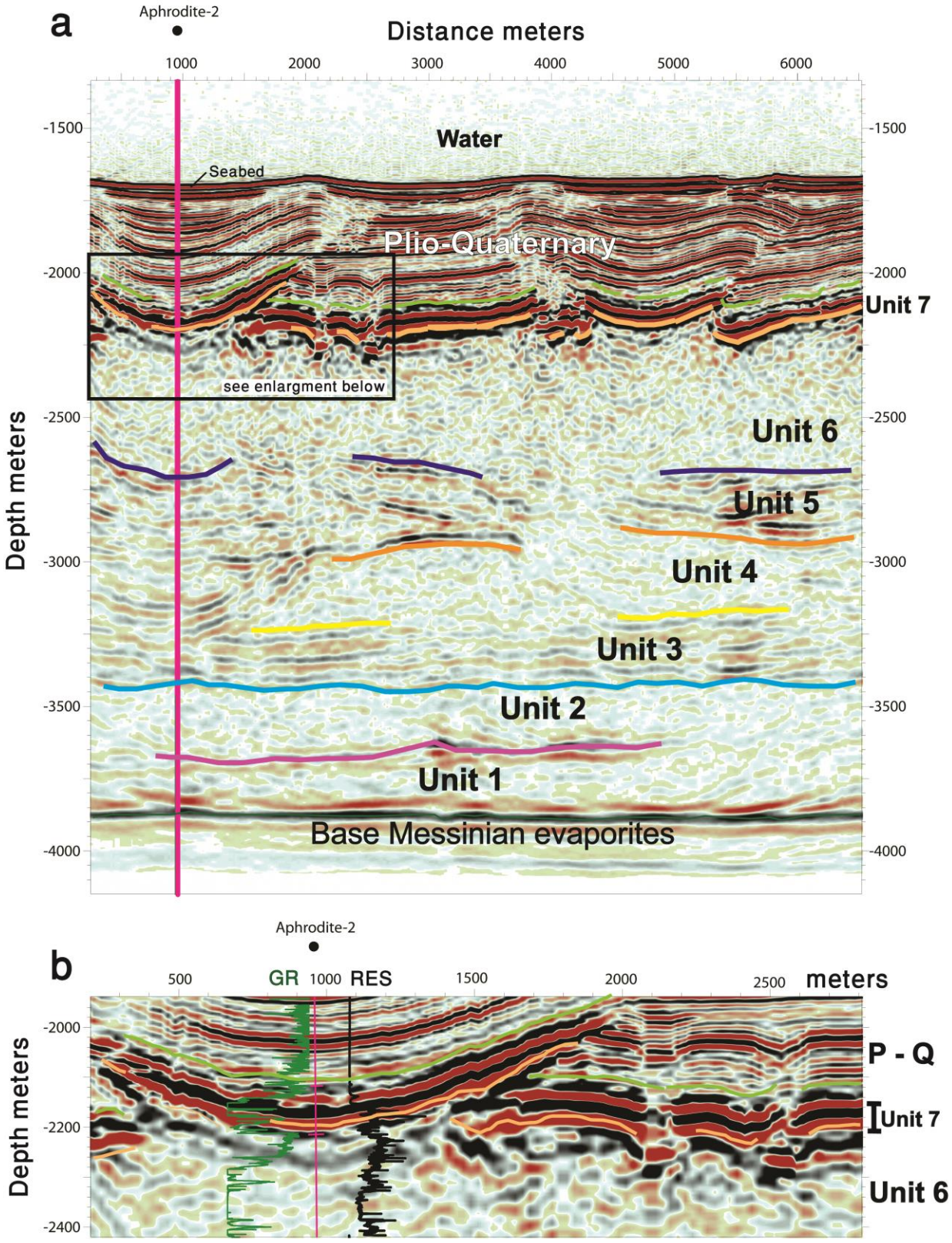

Figure DR2: (a) Seismic stratigraphy near the Aphrodite-2 well showing 7 Messinian units and particularly Unit 7 defined here for the first time. Seabed is a positive (red) peak whereas the base Messinian evaporites is represented by a negative (black) peak. (b) Enlargement of Unit 7 with GR and Res logs of Aphrodite-2 well. Top and base of unit 7 are both represented by positive (red) peaks. Location shown in Fig. DR1.

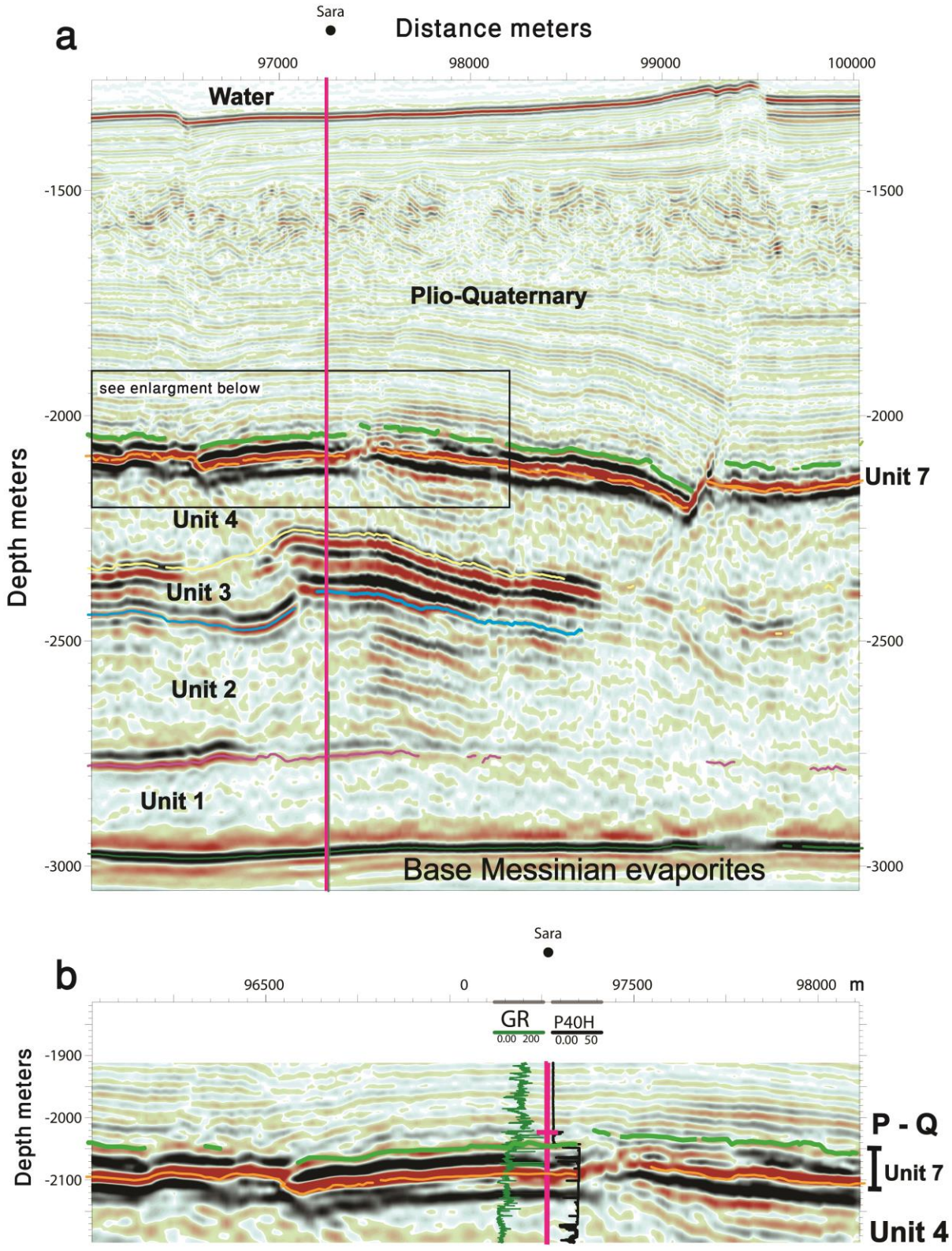

Figure DR3: (a) Seismic stratigraphy near the Sarea-1 well with Unit 7 unconformably lying on Unit 4. Seabed is a positive (red) peak whereas the base Messinian evaporites is represented by a negative (black) peak. (b) Enlargement of Unit 7 with GR and Res logs of Sara-1 well. Top and base of unit 7 are both represented by positive (red) peaks. Location is shown in Fig. DR1.

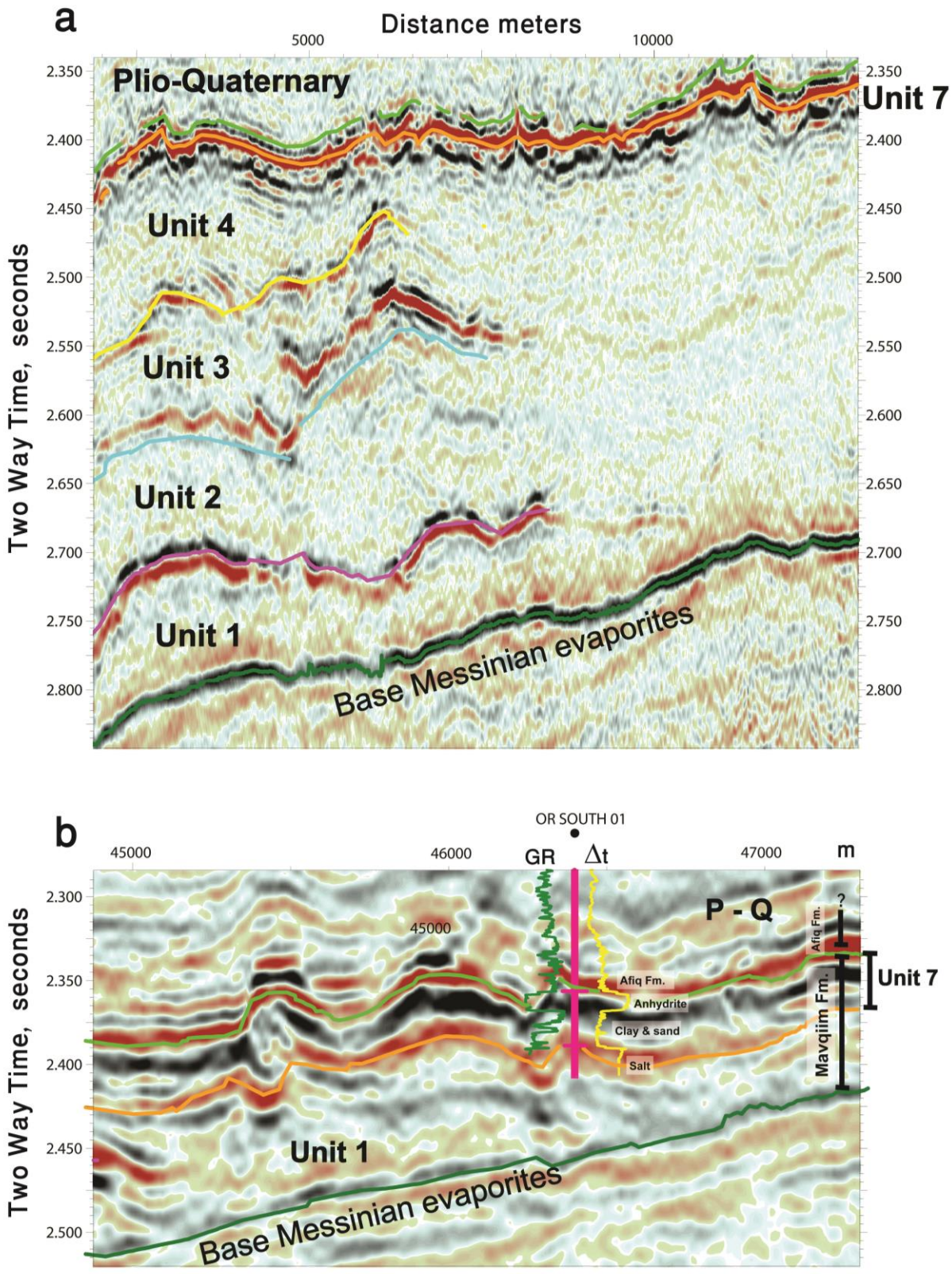

Figure DR4: (a) Seismic stratigraphy in the western (a) and eastern areas of Figure DR1b running along the Afiq Canyon. In (a) Unit 7 unconformably covers Unit 4 whereas in (b) Unit 7 unconformably covers Unit 1 and possibly Unit 2. GR and delta-t logs from Or-South-1 well. Bottom reflector of Unit 7 adjusted to the unconformity truncating salt layers (see Fig. DR5). Location in Fig. DR1.

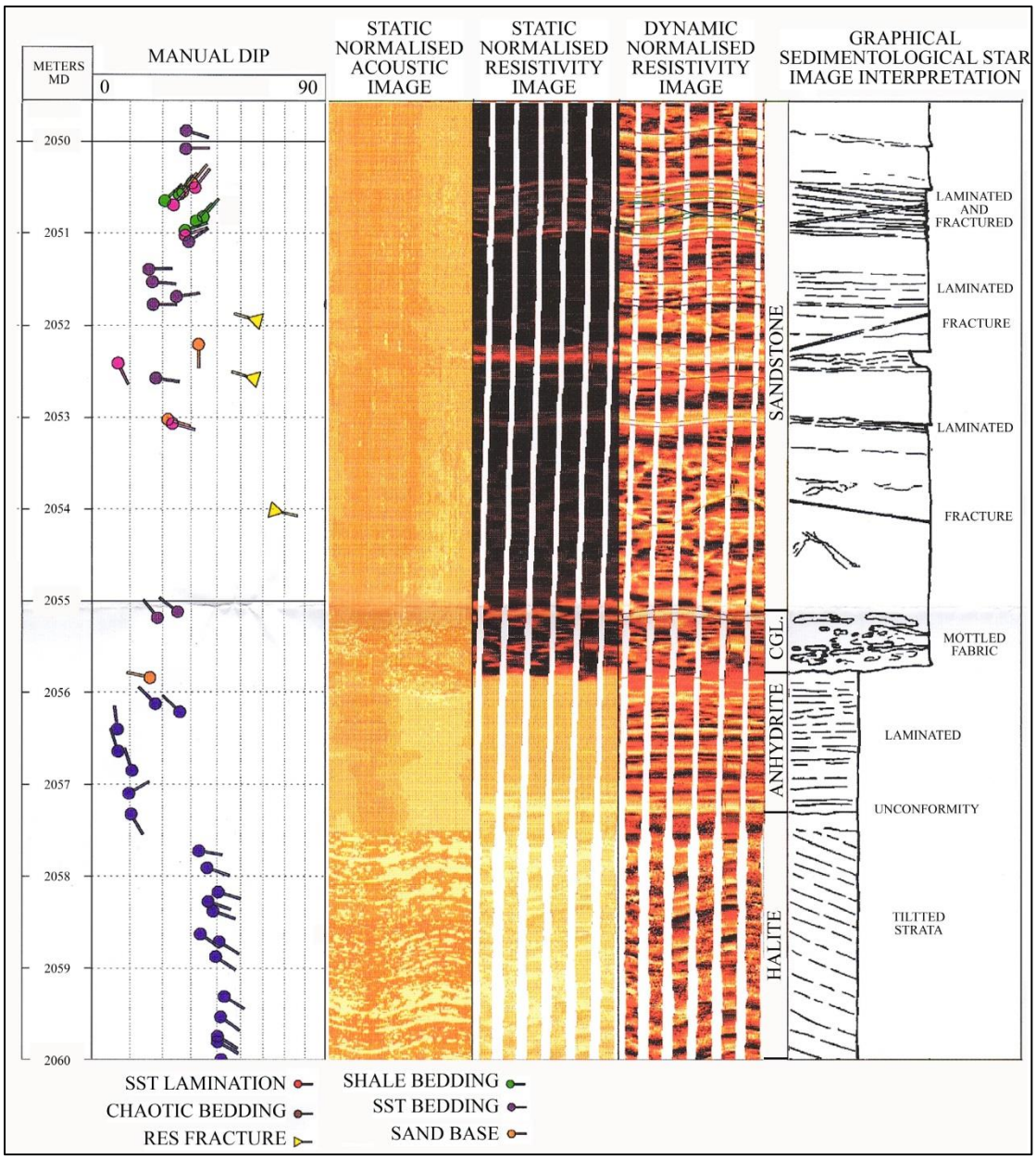

Figure DR5: A borehole image of the bottom part of Or-South-1 well (side track B) showing an angular unconformity between 1.5-m-thick laminated anhydrite layer and a tilted halite section (modified from Hilton, 2001).

$^{87}Sr/^{86}Sr$ analyses

Samples of cuttings from three industrial boreholes (Myra-1, Aphrodite-2 and Or South-1; table DR2) were inspected petrographically both under reflected light-optical microscope and by thin section analysis. The best examples of well-preserved fragments were selected for $^{87}Sr/^{86}Sr$ determination and measured during three different analytical sessions: 11 samples from Myra-1, analyzed in November 2015; 16 samples from Aphrodite-2, in July 2016; and 11 samples from Or South-1, in February 2017. Samples from Myra-1 and Aphrodite-2 essentially consist of clear halite fragments, except for two samples of carbonate mudstone from the lower part and one sample consisting of anhydrite from the top-most portion of Myra-1, while all samples from Or South-1 consist entirely of anhydrite fragments.

Borehole	Sample	Depth (m)	$^{87}Sr/^{86}Sr$	2 S.E.	Rock type
Myra 1	MY1.2380	2380	0.708934	0.000008	Anhydrite
Myra 1	MY1.2465	2465	0.709094	0.000006	Halite
Myra 1	MY1.2675	2675	0.709105	0.000007	Halite
Myra 1	MY1.2875	2875	0.708995	0.000007	Halite
Myra 1	MY1.2930	2930	0.709102	0.000007	Halite
Myra 1	MY1.3035	3035	0.709105	0.000006	Halite
Myra 1	MY1.3095	3095	0.709064	0.000006	Halite
Myra 1	MY1.3195	3195	0.709112	0.000008	Halite
Myra 1	MY1.3306	3306	0.709096	0.000008	Halite
Myra 1	MY1.3365	3365	0.708921	0.000005	Limestone
Myra 1	MY1.3396	3396	0.708927	0.000005	Limestone
Aphrodite 2	APH2.2750	2750	0.709107	0.000010	Halite
Aphrodite 2	APH2.2840	2840	0.709142	0.000009	Halite
Aphrodite 2	APH2.2930	2930	0.709049	0.000009	Halite
Aphrodite 2	APH2.3000	3000	0.709084	0.000009	Halite
Aphrodite 2	APH2.3050	3050	0.709101	0.000014	Halite
Aphrodite 2	APH2.3250	3250	0.709056	0.000008	Halite
Aphrodite 2	APH2.3340	3340	0.709020	0.000009	Halite
Aphrodite 2	APH2.3400	3400	0.708999	0.000009	Halite
Aphrodite 2	APH2.3450	3450	0.709009	0.000008	Halite
Aphrodite 2	APH2.3670	3670	0.709050	0.000009	Halite
Aphrodite 2	APH2.3760	3760	0.709062	0.000010	Halite
Aphrodite 2	APH2.3901	3901	0.708914	0.000010	Halite
Aphrodite 2	APH2.3919	3919	0.709056	0.000014	Halite
Aphrodite 2	APH2.3925	3925	0.709118	0.000015	Halite
Aphrodite 2	APH2.3931	3931	0.708956	0.000008	Anhydrite
Aphrodite 2	APH2.3937	3937	0.708954	0.000007	Anhydrite
Or South 1	OS1.2015	2015	0.708680	0.000008	Anhydrite
Or South 1	OS1.2018	2018	0.708704	0.000009	Anhydrite
Or South 1	OS1.2021	2021	0.708822	0.000008	Anhydrite
Or South 1	OS1.2024	2024	0.708823	0.000008	Anhydrite
Or South 1	OS1.2027	2027	0.708817	0.000010	Anhydrite
Or South 1	OS1.2030	2030	0.708862	0.000011	Anhydrite
Or South 1	OS1.2033	2033	0.708839	0.000008	Anhydrite
Or South 1	OS1.2060	2060	0.708813	0.000009	Anhydrite
Or South 1	OS1.2063	2063	0.708849	0.000011	Anhydrite
Or South 1	OS.12032	2032	0.708847	0.000010	Anhydrite
Or South 1	OS1.2040	2040	0.708776	0.000010	Anhydrite

Table DR2: Results of the $^{87}Sr/^{86}Sr$ analyses

At least 300 mg of halite (10 mg for carbonate and anhydrite) fragments were leached with 1M ammonium acetate in order to remove exchangeable Sr and then washed and centrifuged with MilliQ water. After drying, the carbonate and anhydrite samples were dissolved in 3M HNO_3. The halite samples were first dissolved in MilliQ water and the insoluble

particles removed. The supernatant solutions were then centrifuged, evaporated to dryness and the re-precipitated halite was dissolved in 3M HNO_3. Strontium was seperated and preconcentrated using Eichrom Sr-SPEC resin SR-B50-A (100-150 μm), following the procedure described in Palmiotto et al. (2013). Final solutions were adjusted to a concentration of 4% w/w HNO_3 and analyzed within a few days.

Strontium isotope ratios were obtained using a multi collector inductively coupled plasma mass spectrometer (*HR-MC-ICPMS Thermo ScientificTM Neptune*), housed at CIGS (Centro Interdipartimentale Grandi Strumenti, University of Modena and Reggio Emilia). Strontium concentration was previously determined using a quadrupole inductively coupled plasma mass spectrometer (*ICPMS X Series II, Thermo Fisher Scientific*). During all analytical sessions the sensitivity on the ^{88}Sr peak for 200 ppb Sr was > 10 V with the blank (4% w/w HNO_3) being < 0.03 V. The strontium isotope standard NIST SRM 987 (accepted $^{87}Sr/^{86}Sr$ value of 0.710260 ± 0.000020; Ehrlich et al., 2001) was used as an external standard. Samples, standards and blank solutions were analyzed using the instrumental configuration and correction parameters reported in Reghizzi et al. (2017). Repeated measurements of the NIST SRM 987 standard yielded a mean value of 0.710274 ± 0.000013 (2 S.D., n = 12) in November 2015; 0.710272 ± 0.000029 (2 S.D., n = 20) in July 2016; and 0.710259 ± 0.000015 (2 S.D., n = 15) in February 2017. The internal precision of individual standard analyses in all sessions varied between 0.000005 and 0.000010 (2 S.E.). The average internal uncertainty for all samples was 0.000009 (2 S.E.), with minimum and maximum values of 0.000006 and 0.000015, respectively.

References

Ehrlich, S., Gavrieli, I., Dor, L., Halicz, L., 2001. Direct high-precision measurements of the 87Sr/86Sr isotope ratio in natural water, carbonates and related materials by multiple collector inductively coupled plasma mass spectrometry (MC-ICP-MS). Journal of Analytical Atomic Spectrometry, 16, 1389-1392.

Feng, Y. E., Yankelzon, A., Steinberg, J., and Reshef, M., 2016, Lithology and characteristics of the Messinian evaporite sequence of the deep Levant Basin, eastern Mediterranean: Marine Geology, v. 376, p. 118-131.

Hilton, V. C., 2001, BG International offshore Israel, Med Yavne license: Or-1 & Or Shouth-1, Structural and sedimentological interpretation of STAR data, core sedimentology and petrography of core samples. Baker Atlas GEOScience, Final Report # ZSL-00-075, 32 p.

Palmiotto, C., Corda, L., Ligi, M., Cipriani, A., Dick, H.J.B., Douville, E., Gasperini, L., Montagna, P., Thil, F., Borsetti, A.M., Balestra, B., and Bonatti, E., 2013. Nonvolcanic tectonic islands in ancient and modern oceans. Geochemistry, Geophysics, Geosystems 14(10):4698–4717.

Reghizzi, M., Gennari, R., Douville, E., Lugli, S., Manzi, V., Montagna, P, Roveri, M., Sierro, F. J., Taviani, M., 2017. Isotope stratigraphy ($^{87}Sr/^{86}Sr$, $\delta^{18}O$, $\delta^{13}C$) of the Sorbas basin (Betic Cordillera, Spain): paleoceanographic evolution across the onset of the Messinian salinity crisis. Palaeogeography, Palaeoclimatology, Palaeoecology 469, 60-73.